

Piezo-catalytic in-site H_2O_2 generation and activation across wide pH range to drive hydroxyl radical-mediated pollutant degradation

Received: 21 March 2025

Accepted: 13 August 2025

Published online: 25 August 2025

Jing Xu^{1,4}, Kaiye Gu^{1,4}, Peifang Wang¹, Pengfei Cheng², Huinan Che¹, Chunmei Tang³, Kan Zhang²✉ & Yanhui Ao¹✉

Hydroxyl radicals ($\cdot\text{OH}$) is one of the most important reactive oxygen species (ROSs) for organic pollution controlling in advanced oxidation processes, while its production suffers from numerous H_2O_2 addition and narrow pH range in generally used Fenton reaction. Herein, we demonstrate a BiOI/O_3 (BIO) piezo-catalyst loaded with $\gamma\text{-FeOOH}$ nanoparticles (FNPs) (BF) that can convert O_2 to $\cdot\text{OH}$ in a wide pH condition without external H_2O_2 addition under ultrasonication. It is found that the robust interfacial interaction facilitates rapid electron migration from BIO to FNPs, enabling two-electron O_2 reduction into H_2O_2 at the FNPs site, while the leaving behind piezo-holes to perform two-electron water oxidative H_2O_2 generation on BIO. Because the electron-rich nature of FNPs favors the H^+ adsorption that contributes a surface acidic micro-environment, the produced H_2O_2 can be in-situ catalyzed into $\cdot\text{OH}$ in either neutral or even alkaline conditions with a great stability. Finally, the optimal BF can achieve either an impressive $\cdot\text{OH}$ yield of $38.1 \mu\text{M h}^{-1}$ or a high H_2O_2 yield of $522.0 \mu\text{M h}^{-1}$ by regulating the FNPs loading mass, which enables dual capabilities of rapid organic pollutants degradation and H_2O_2 production in a wide pH condition.

Hydroxyl radicals ($\cdot\text{OH}$), are among the most powerful reactive oxygen species (ROS), offering exceptional potential in environmental remediation due to their high oxidation potential (2.8 V) and near-diffusion-limited reaction kinetics^{1–5}. However, traditional $\cdot\text{OH}$ generation strategies, such as Fenton and Fenton-like systems, face critical limitations due to their strict reliance on acidic conditions (pH 2–4) and continuous external supplementation of hydrogen peroxide (H_2O_2), driving up operational costs and limiting scalability^{6–8}. Overcoming the dual dependency on pH and H_2O_2 to achieve efficient $\cdot\text{OH}$ synthesis remains a pivotal challenge.

To address these issues, advanced catalytic approaches, including photocatalysis and piezocatalysis, have been investigated^{9,10}, which theoretically enable direct $\cdot\text{OH}$ generation through water splitting ($\text{H}_2\text{O} + \text{energy} \rightarrow \cdot\text{OH} + \cdot\text{H}$)¹¹ or water oxidation ($\text{H}_2\text{O} + \text{h}^+ \rightarrow \cdot\text{OH}$, (2.38 V vs. RHE))¹ under energy input (e.g., light irradiation, mechanical stress). Yet these approaches are constrained by slow reaction rates, high reaction energy barriers, and low radical yields^{12,13}. Another emerging approach focuses on in-situ H_2O_2 production via two-electron water oxidation reactions (2e^- WOR) ($2\text{H}_2\text{O} + 2\text{h}^+ \rightarrow \text{H}_2\text{O}_2 + 2\text{H}^+$ (1.76 V vs. RHE))¹⁴ or two-electron oxygen reduction reactions (2e^- ORR) ($\text{O}_2 + 2\text{e}^-$

¹Key Laboratory of Integrated Regulation and Resource Development on Shallow Lakes, Ministry of Education, College of Environment, Hohai University, Nanjing, China. ²School of Materials Science and Engineering, Nanjing University of Science and Technology, Nanjing, China. ³College of Science, Hohai University, Nanjing, China. ⁴These authors contributed equally: Jing Xu, Kaiye Gu. ✉e-mail: zhangkan@njut.edu.cn; andyao@hhu.edu.cn

+ 2H⁺ → H₂O₂ (0.68 V vs. RHE)^{15–17}, followed by H₂O₂ activation to produce ·OH¹⁸. Clearly, an efficient self-Fenton catalyst should theoretically possess both 2e[−] WOR and 2e[−] ORR to maximize the yield of H₂O₂, but its development faces challenges. Besides, while some self-sustaining systems avoid external H₂O₂ consumption, the slow kinetics of high-valent Fenton-active metals (e.g., Fe^{III}, Cu^{II}, Co^{III}) transitioning to their low-valent states (Fe^{II}, Cu^I, Co^{II})^{19–27} still constrains H₂O₂ activation efficiency, ultimately impairing pollutant degradation performance.

Herein, we present a BiOIO₃/FeOOH (BF) piezo-catalyst fabricated via an impregnation hydrolysis process that achieves one-step ·OH generation with high efficiency and pH-tolerance. Robust interfacial interaction between BiOIO₃ (BIO) and FeOOH nanoparticles (FNPs) promotes rapid electron transfer, rendering the FNPs electron-rich during piezo-catalysis. Under mechanical stress, adsorbed O₂ on FNPs is reduced to H₂O₂ via a 2e[−] transfer pathway, while leaving behind holes on BIO that are responsible for 2e[−] WOR to produce H₂O₂. The in situ-generated H₂O₂ is then directly activated by FNPs to produce ·OH, eliminating the need for additional metal ion. Moreover, the electron-enriched FNPs induce localized H⁺ accumulation, creating an acidic microenvironment that enables efficient pollutant removal across a

wide pH range. This innovative approach not only simplifies the reaction pathway but also enhances catalytic efficiency, offering a cost-effective and versatile solution for environmental applications.

Results and discussion

Synthesis and characterization

A straightforward one-step hydrothermal method was used to prepare BIO nanosheets (Supplementary Fig. 1a, b and Supplementary Fig. 2)²⁸. X-ray diffraction (XRD) spectrum indicates its crystal configuration as pure phase BIO (Supplementary Fig. 3b). The well-aligned diffraction spots and atomic phases in the selected area electron diffractogram (SAED) and inverted fast Fourier transform (FFT) in Supplementary Fig. 1c reveal the perfect single-crystal structure of the BIO nanosheets. The layer spacing with d-spacing of 0.283 and 0.287 nm is assigned to the (200) and (002) crystal surfaces of BIO, respectively. BIO/γ-FeOOH (BF) was synthesized from BIO through a convenient impregnation hydrolysis strategy (Fig. 1a). It originates from the controllable hydrolysis of Fe^{III} in an acidic medium, which initially forms critical nuclei containing a small number of iron atoms on BIO in the limitation of pH and further polymerizes to 3–5 nm FeOOH nanoparticles with

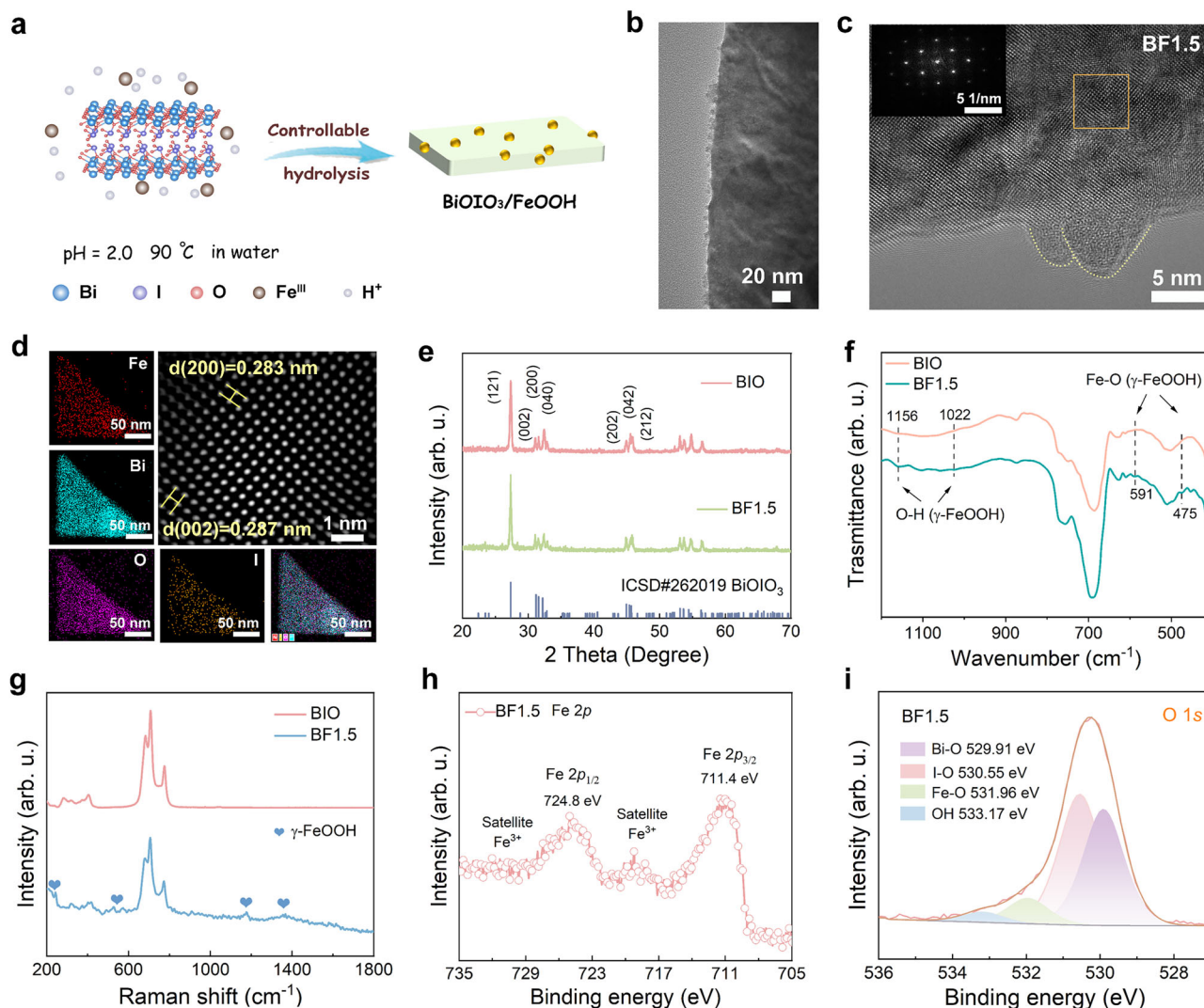


Fig. 1 | Synthesis and characterization of BiOIO₃/γ-FeOOH (BF) catalysts.

a Schematic synthesis of BiOIO₃/γ-FeOOH (BF) catalysts. **b** Transmission electron microscope (TEM) and **c** high resolution transmission electron microscopy (HRTEM) images of BF1.5 (inset, the selected area electron diffractogram (SAED) of BF1.5). **d** Corresponding inverse fast Fourier transform (FFT) pattern of yellow box

area in (c), and elements mapping of Bi, I, O and Fe elements in BF1.5. **e** X-ray diffraction (XRD), **f** Fourier transform infrared spectroscopy (FTIR) and **g** surface-enhanced Raman spectroscopy (SERS) spectra of BIO and BF1.5. X-ray photoelectron spectroscopy (XPS) spectra of **h** Fe 2p and **i** O 1s in BF1.5.

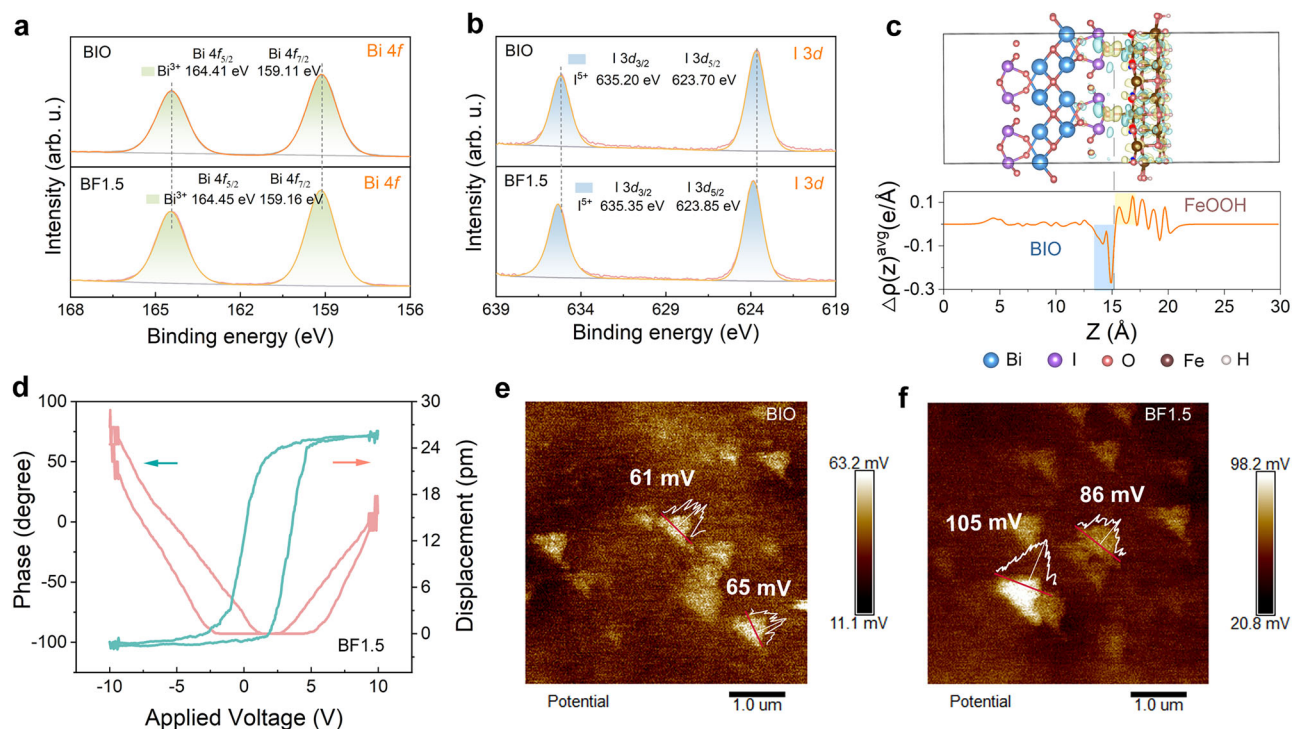


Fig. 2 | Characterizations of charge redistribution and piezoelectric performance. **a** Bi 4f and **b** I 3d XPS spectra of BIO and BF1.5. **c** The planar average charge density differences of BF. Yellow denotes electron accumulation; blue indicates

electron depletion. The iso-surface of density was set to 0.002 e Å⁻³. **d** The butterfly amplitude loop and phase curves of BF1.5. Surface piezo-potentials of **e** BIO and **f** BF1.5.

elevated temperatures (Fig. 1b, c and Supplementary Fig. 3a)^{29–32}. The limited size of FeOOH nanoparticles can markedly decrease the transport distance of piezo-electron to the surface reaction sites, favoring the catalytic activity^{33–36}. The lattice fringes corresponding to the (200) and (002) crystal planes of BIO are observed in inverse FFT spectra of the BF (Fig. 1d), indicating that the surface loading of FeOOH does not alter the single-crystal structure of BIO. This finding is further corroborated by the XRD test results in Fig. 1e and Supplementary Fig. 3b. The highly ordered lattice structure is conducive to the macroscopic superposition of piezoelectric polarity.

Elemental mapping reveals the uniform distribution of Fe elements across the BIO nanosheets in Fig. 1d. Inductively coupled plasma optical emission spectroscopy (ICP-OES) analysis revealed that the Fe content in BF1.5 is about 0.43 wt%. Fourier transform infrared (FTIR) and surface-enhanced Raman spectroscopy (SERS) confirmed the presence of iron on the BIO surface in the form of γ-FeOOH. Specifically, in the FTIR spectra (Fig. 1f), the peaks at 1156 and 1022 cm⁻¹ correspond to the O-H bending vibrations of γ-FeOOH, while the peaks at 591 and 475 cm⁻¹ are attributed to the Fe-O bond vibrations of γ-FeOOH³⁷. Given the low Fe loading, the SERS was employed to amplify the Fe-species signal on the BIO surface. As shown in Fig. 1g, the new characteristic peaks at 245, 526, 1176 and 1361 cm⁻¹ in BF are consistent with γ-FeOOH³⁸. Besides, X-ray photoelectron spectroscopy (XPS) measure was conducted to explore the surface chemical state of the samples. As expected, the XPS survey spectra of BF reveal characteristic peaks for Fe 2p, along with peaks for Bi 4f, I 3d and O 1s belonging to BIO (Supplementary Fig. 4). Notably, the Fe 2p core-level spectrum of BF1.5 (Fig. 1h) shows two major Fe^{III} peaks at about 711.4 and 724.8 eV, as well as two minor Fe^{III} satellite peaks at around 718.4 and 731.8 eV³⁹. In Fig. 1i, the O 1s XPS spectrum of BF was divided into four diffraction peaks located around 529.91, 530.55, 531.96 and 533.17 eV, which correspond to the binding energies of Bi-O, I-O, Fe-O and a surface hydroxyl group (OH), respectively^{40,41}. Obviously, the introduced Fe^{III} is bonded to the O elements. Accordingly, the as-prepared

BF is composed of single-crystalline BIO and surface γ-FeOOH nanoparticles (FNPs), where the long-range well-ordered crystal structure of BIO can facilitate the superposition of piezo-polarization, while the surface FNPs are expected to provide more highly active sites for catalytic reaction^{42,43}.

Charge transfer properties and piezoelectricity analysis

The strongly coupled interface between BIO and FNPs in BF was first investigated by XPS fine spectra. It is evident that the incorporation of FNPs induces shifts toward higher binding energies in the characteristic peaks of Bi 4f, I 3d, and O 1s (Fig. 2a, b and Supplementary Fig. 5), indicating a decrease in the electron cloud density surrounding these elements. This implies a robust interfacial interaction between BIO and FNPs, driving interfacial electron redistribution from BIO to FNPs. To gain insight into the charge transfer patterns at the BIO-FNPs interface, the planar average charge density differences were plotted. In Supplementary Fig. 6, the optimized electronic structure of the BF shows that FNPs are tightly bound to BIO through Fe-O bonds, consistent with the FTIR and XPS O 1s spectra of BF1.5. Figure 2c illustrates the accumulation (yellow) and depletion (blue) of electrons at FNPs and BIO, respectively. Clearly, the interfacial interaction results in electron modulation in BF, wherein FNPs extract electrons from BIO, becoming an electron-rich entity. This feature is beneficial for the subsequent O₂ reduction and H₂O₂ activation with FNPs as the reactive site.

Given that the piezo-catalytic reactivity of the samples is directly related to their piezoelectric response, the intrinsic piezoelectricity of BIO and BF was evaluated by piezoelectric force microscopy (PFM). In Fig. 2d and Supplementary Figs. 7, 8, under applied bias voltages from -10 to 10 V, both BIO and BF underwent continuous surface deformation, accompanied by the formation of localized hysteresis loops and pronounced 180° phase inversion, evidencing the piezoelectric properties of the materials. The maximum effective piezoelectric coefficient (d₃₃) values based on the amplitude loops BIO and BF are 2.31 and 2.96 pm/V, respectively (Supplementary Fig. 8c), clarifying the

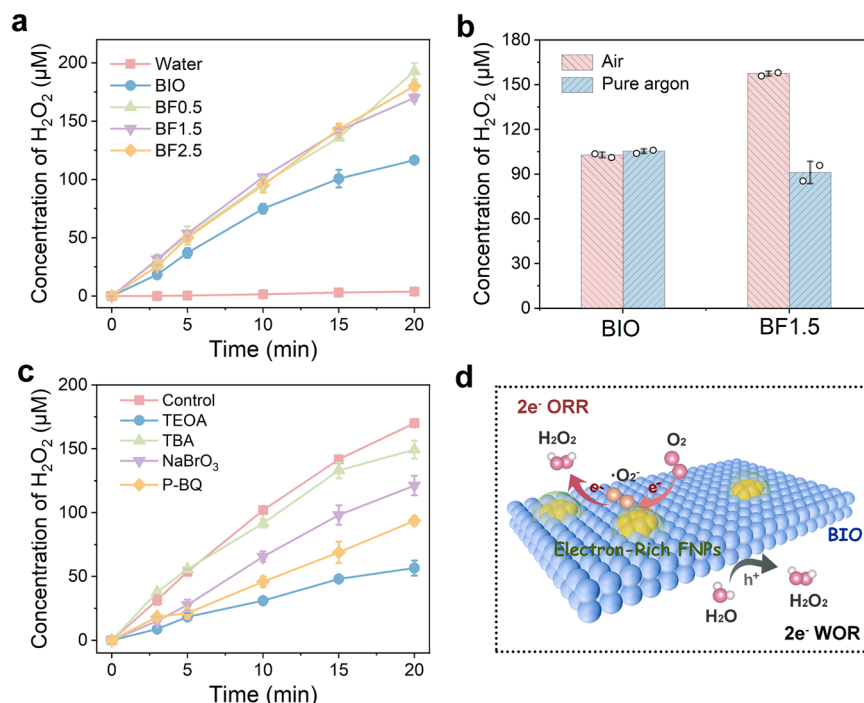


Fig. 3 | Dual-channel H₂O₂ synthesis performance and mechanism analysis.

a Time profiles of H₂O₂ evolution within 20 min in different systems. **b** H₂O₂ yield of BIO and BF1.5 in pure water/air and pure water/Ar in a sealable reactor at 20-min reaction time. **c** Impact of various capture reagents on H₂O₂ evolution by BF1.5. (**1**–**4**–

triethanolamine (TEOA), tert-butanol (TBA), sodium bromates (NaBrO₃) and benzoquinone (p-BQ) for piezo-holes, ·OH, piezo-electrons and ·O₂⁻ capture, respectively). **d** Mechanism of H₂O₂ generation over BF1.5. The error bars in (**a**, **b**, **c**) represent the standard deviations from two parallel measurements.

significantly enhanced piezo-response of BF with the introduction of FNPs. Moreover, the surface potential of catalysts under mechanical stress was tested using Kelvin Probe Force Microscopy (KPFM). In Fig. 2e, f, the KPFM results reveal that BF1.5 exhibits a significantly higher surface potential compared to pristine BIO. This enhancement is likely attributed to interfacial charge redistribution between FeOOH and BIO, which induces additional dipole formation and strengthens the overall polarization. Such enhanced polarization not only promotes efficient separation of piezo-induced charge carriers but also contributes to the improved piezo-catalytic activity of the material.

In-situ H₂O₂ generation activity

The in situ H₂O₂-production activity of the as-prepared samples was systematically investigated. As shown in Fig. 3a, the H₂O₂ yield of BIO in pure water was approximately 116 μM in 20 min. In contrast, the introduction of electron-rich FNPs resulted in increases in the H₂O₂ yields of BF systems, with BF1.5 reaching 174 μM in 20 min (1.5 times that of BIO), demonstrating FNPs as efficient H₂O₂ production sites. Control experiments in a customized sealable reactor were then conducted to reveal the origin of H₂O₂. As depicted in Fig. 3b, the H₂O₂ yield of BIO in pure water/air is approximately 103 μM. When the air was completely replaced by Ar, the H₂O₂ yield remained nearly unchanged at 105 μM, indicating that BIO is highly selective for the 2e⁻ WOR pathway (Supplementary Fig. 11), as proved in our previous studies⁴⁴. Notworthily, BF1.5 exhibited much high H₂O₂ yields in pure water/air (157 μM), while also maintaining high activity for H₂O₂ generation in pure water/Ar (91 μM). It can be inferred that in addition to H₂O molecules, dissolved O₂ is another crucial feedstock for H₂O₂ synthesis in the BF1.5 system.

To give more details of the BF1.5 for H₂O₂ production, a series of capture experiments were conducted. In Fig. 3c and Supplementary Fig. 13, the addition of TEOA significantly inhibited H₂O₂ production, confirming the 2e⁻ WOR capacity for H₂O₂ production in BF1.5.

Additionally, the addition of TBA slightly suppressed the H₂O₂ generation of BF1.5, indicating that H₂O₂ is not generated by the 1e⁻ WOR (H₂O + h⁺ → ·OH, ·OH + ·OH → H₂O₂). Moreover, H₂O₂ yield decreased remarkably when NaBrO₃ and p-BQ were used to capture electrons and ·O₂⁻, respectively. This confirms that indirect 2e⁻ ORR is another vital pathway for H₂O₂ synthesis by BF1.5, where ·O₂⁻ serves as a key intermediate (O₂ + e⁻ → ·O₂⁻, ·O₂⁻ + e⁻ + 2H⁺ → H₂O₂)⁴⁵.

To further intuitively evaluate the electron transfer behavior of BF1.5 during the H₂O₂ synthesis process, rotating ring-disk electrode (RRDE) measurements were conducted. The oxygen reduction pathway of BF1.5 was first examined⁴⁶. As shown in Supplementary Fig. 14a, b, a cathodic reduction current was detected at the disk electrode during the negative potential sweep, while a corresponding anodic current was simultaneously observed at the ring electrode. This indicates that H₂O₂ generated at the disk rapidly diffused to the ring, where it was oxidized. The calculated average electron transfer number (*n*) and H₂O₂ selectivity for BF1.5 were 2.37 and 81.3%, respectively, suggesting that the ORR proceeds predominantly via a 2e⁻ pathway. To elucidate the water oxidation behavior of BF1.5, RRDE measurements were also performed under anodic conditions⁴⁶. In this setup, the potential of the rotating disk electrode was scanned from 0.8 to 2.1 V (vs. Ag/AgCl), while the Pt ring electrode was held at a constant potential of -0.23 V to monitor potential O₂ generation via 4e⁻ WOR. As shown in Supplementary Fig. 15a, the disk current began to increase when the applied potential exceeded 1.2 V, indicating the onset of water oxidation on the BF1.5-modified disk. Notably, no cathodic current was detected at the ring electrode under these conditions, ruling out the occurrence of the four-electron pathway that leads to O₂ evolution. However, when the ring potential was adjusted to +0.6 V (vs. Ag/AgCl), a distinct anodic current was observed, which is attributed to the oxidation of H₂O₂ at the Pt ring (Supplementary Fig. 15b). Obviously, H₂O₂ synthesis in BF1.5 primarily occurs through dual channels process, where H₂O molecules are oxidized on BIO

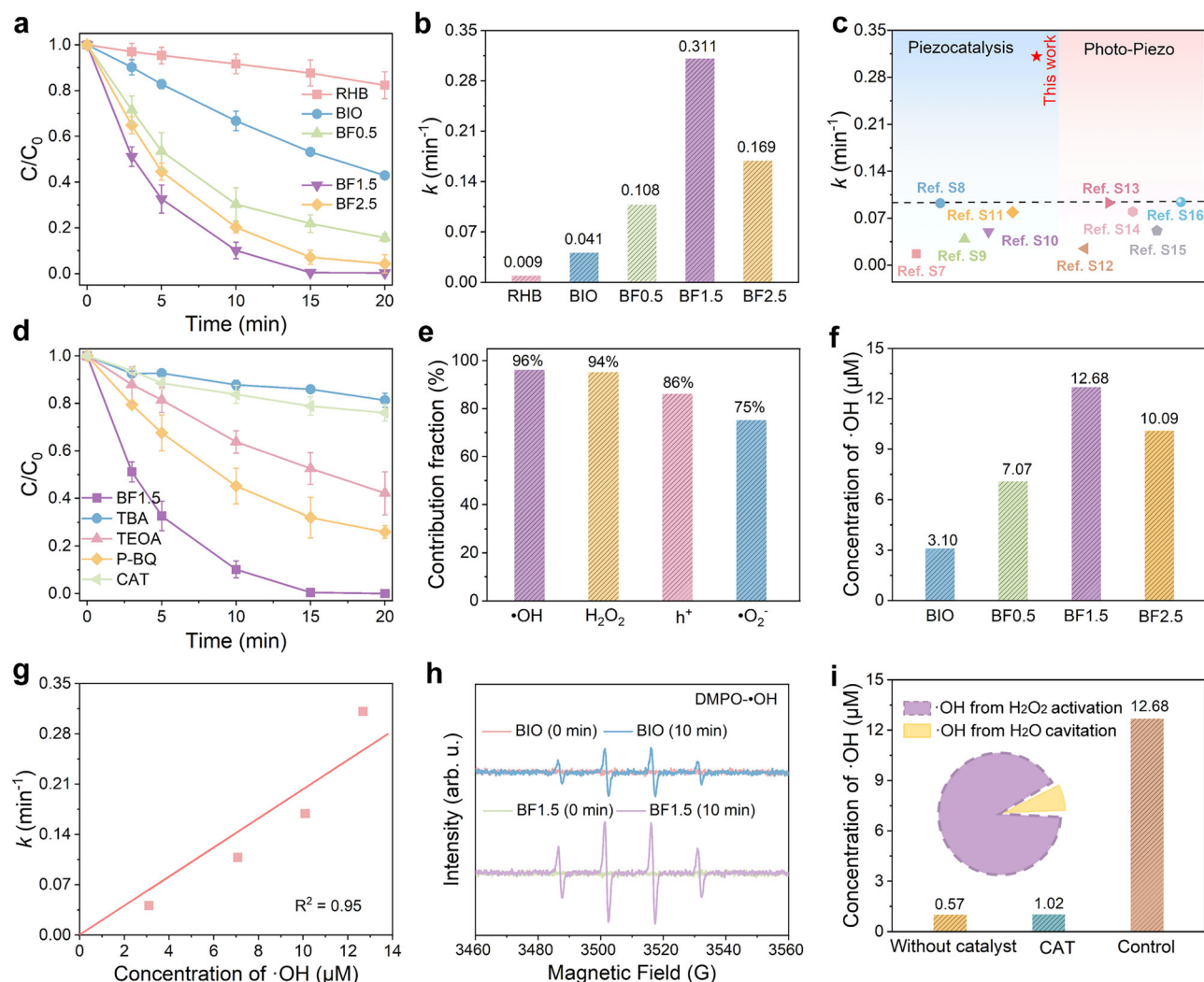


Fig. 4 | Rapid pollutant removal performance and mechanism analysis.

a Rhodamine B (RhB) degradation with different catalysts and **b** the corresponding pseudo-first-order kinetic constant (k) within 15 min. **c** Comparison of k values for RhB degradation by catalysts in recent studies. The data points (arranged from left to right) correspond to the reference numbers 7–16 provided in the supplementary information, and more detailed parameters are given in Supplementary Table 1, including sample names, k values, etc. **d** Impact of various capture reagents on RhB degradation by BF1.5 (tert-butanol (TBA), catalase (CAT), 1,4-triethanolamine

(TEOA) and benzoquinone (p-BQ) for $\cdot\text{OH}$, H_2O_2 , piezo-holes and $\cdot\text{O}_2^-$ trapping, respectively). **e** Contribution of different reactive oxygen species to RhB degradation in BF1.5 system. **f** $\cdot\text{OH}$ yield within 20 min in different systems. **g** Linear correlation between $\cdot\text{OH}$ yield and k values in BIO and BF systems. **h** ESR spectra of DMPO- $\cdot\text{OH}$ in BIO and BF1.5 system. **i** $\cdot\text{OH}$ yield within 20 min in the BF1.5 system under various reaction parallel conditions. The error bars in (**a**, **d**) represent the standard deviations from two parallel measurements.

nanosheets for $2e^-$ WOR, and O_2 molecules are reduced on electron-rich FNPs for indirect $2e^-$ ORR (Fig. 3d). The emerging indirect $2e^-$ ORR can be attributed to the introduction of electron-rich FNPs sites.

Hydroxyl radicals-dominated pollutant removal

The piezo-catalytic performance of catalysts was then evaluated with RhB as the model pollutant. As shown in Fig. 4a, the degradation rate of RhB was only 12.3% in 15 min without catalysts. With the addition of BIO, the degradation rate increased to 47.1%. In stark contrast, the degradation efficiencies of RhB in BF systems were significantly higher, with BF1.5 achieving nearly complete RhB degradation (99.6%) within 15 min. Its degradation kinetic constant (0.311 min^{-1}) was approximately 7.6 times that of BIO (Fig. 4b and Supplementary Fig. 16), outperforming most reported piezo-catalytic systems and even some photo-piezo-coupled systems (Fig. 4c and Supplementary Table 1). Apparently, massive reactive species are generated in BF1.5 system, primarily due to the electron-rich FNPs centers, which serve as active sites for catalytic reactions.

To identify the most active reactive species, trapping experiments were conducted. As shown in Fig. 4d, e, the addition of TBA significantly inhibited RhB degradation, confirming that $\cdot\text{OH}$ is the primary active species, contributing 96% to the overall degradation. The inhibition observed with catalase (CAT) followed a similar trend, highlighting the crucial role of H_2O_2 , which contributes 94%, nearly equal to that of $\cdot\text{OH}$. Additionally, TEOA and p-BQ reduced the degradation contributions to 86% and 75%, respectively, suggesting smaller but still significant effects from piezo-holes and $\cdot\text{O}_2^-$. Considering the decisive role of $\cdot\text{OH}$ in pollutant degradation, we performed $\cdot\text{OH}$ quantitative experiments to explore the sources of performance differences across catalytic systems. As shown in Fig. 4f and Supplementary Fig. 18, FNPs significantly facilitates the $\cdot\text{OH}$ production, with BF1.5 exhibits the highest yield of $12.7 \mu\text{M}$ in 20 min ($38.1 \mu\text{M h}^{-1}$), 4.1 times greater than that of BIO. Intriguingly, linear fitting revealed a positive correlation between $\cdot\text{OH}$ yield (x) and the pollutant degradation rate of catalysts (y) (Fig. 4g) ($y = 0.02x$), validating BIO and BF as $\cdot\text{OH}$ -dominated systems. EPR analysis further

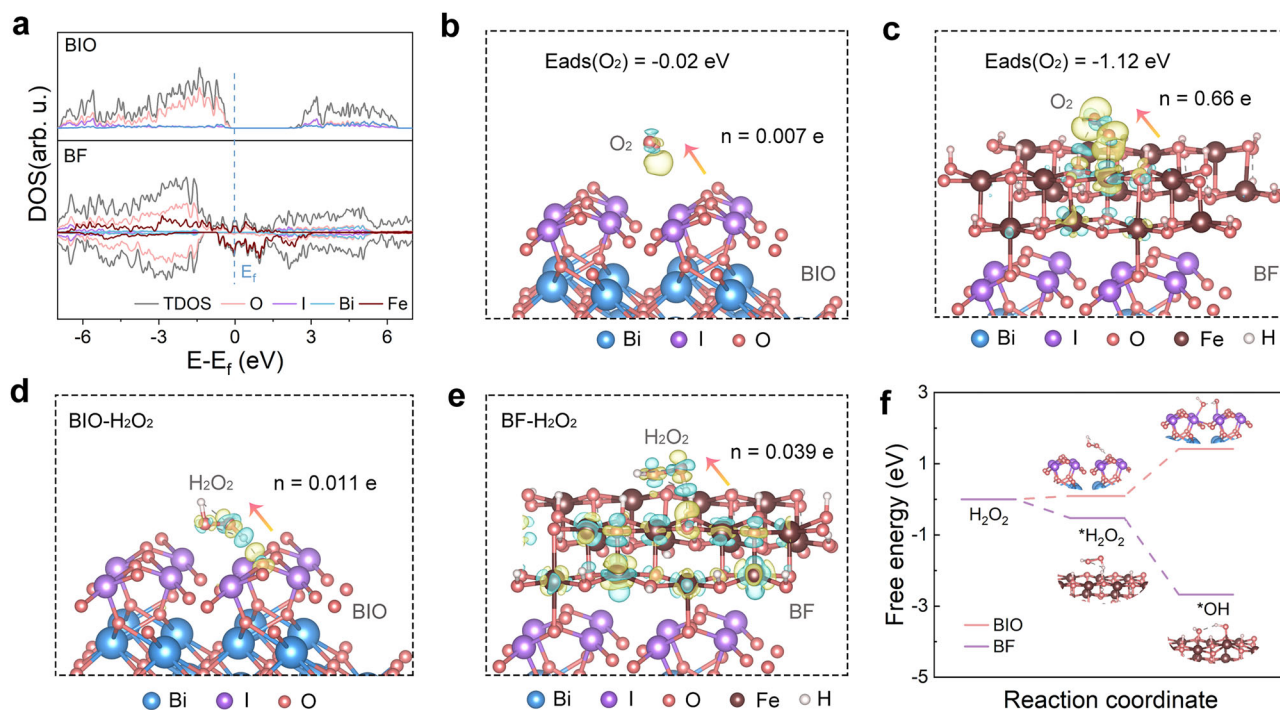


Fig. 5 | DFT calculation for the $\cdot\text{OH}$ evolution. **a** The density of states (DOS) of BIO and BF. Adsorption energy (E_{ads}) and charge density difference distribution for **b** BIO and **c** BF with O_2 adsorbed. Yellow denotes electron accumulation; blue indicates electron depletion. The iso-surface of density for both were set to

$0.0004 \text{ e} \text{ \AA}^{-3}$ and $0.004 \text{ e} \text{ \AA}^{-3}$, respectively. Differential charge density distributions and electron transfer numbers for **d** BIO and **e** BF in H_2O_2 activation, the iso-surface of density is set to $0.004 \text{ e} \text{ \AA}^{-3}$. **f** The free energy for activation of H_2O_2 to $\cdot\text{OH}$ on BIO and BF.

assess the DMPO- $\cdot\text{OH}$ signal intensity in different systems. As depicted in Fig. 4h, the DMPO- $\cdot\text{OH}$ peak intensity of BF1.5 was significantly boosted compared to that of BIO, further implying that the introduction of FNPs centers initiates rapid and efficient generation of $\cdot\text{OH}$.

Total organic carbon (TOC) analysis revealed a high mineralization efficiency of 53.9% for RhB within 15 min in the BF1.5 system (Supplementary Fig. 19), demonstrating its excellent degradation capability. Additionally, liquid chromatography-mass spectrometry (LC-MS) was employed to identify possible intermediate products formed during RhB degradation (Supplementary Fig. 20, 21). Based on further Fukui function calculations (Supplementary Fig. 22, 23 and Supplementary Table 3), a plausible degradation pathway was proposed (Supplementary Fig. 24). As illustrated, RhB undergoes a series of degradation steps including N-demethylation, deamination, dealkylation, decarboxylation, chromophore cleavage, ring opening, and eventual mineralization. These results clearly indicate that RhB is efficiently decomposed through $\cdot\text{OH}$ -driven oxidative processes, highlighting the promising application potential of the BF1.5 system in pollutant degradation.

To identify the origin of $\cdot\text{OH}$ in BF1.5 systems, a series of controlled experiments were conducted. The $\cdot\text{OH}$ yield from cavitation in pure water (without catalyst) was first measured. In Fig. 4i, ultrasonic cavitation in pure water generates trace amounts of $\cdot\text{OH}$ ($0.57 \mu\text{M}$ in 20 min, $\text{H}_2\text{O} + \text{H}_2\text{O}_2$) $\rightarrow \cdot\text{OH} + \cdot\text{H}$, demonstrating that the cleavage of H_2O molecules contributes minimally to $\cdot\text{OH}$ generation in BF1.5. The role of H_2O_2 in $\cdot\text{OH}$ production was then assessed by adding CAT, which specifically catalyzes the decomposition of H_2O_2 into H_2O and O_2 ($2\text{H}_2\text{O}_2 \rightarrow 2\text{H}_2\text{O} + \text{O}_2$)⁴⁷. As shown, the decomposition of H_2O_2 by CAT caused a dramatic reduction in $\cdot\text{OH}$ yield, from 12.68 to $1.02 \mu\text{M}$, confirming that H_2O_2 activation is the primary pathway for $\cdot\text{OH}$ generation. This also explains the sharp decline in the pollutant degradation rate upon H_2O_2 capture.

In addition, to elucidate the role of FeOOH in H_2O_2 activation, we introduced CAT into the BF1.5 system to compete with FeOOH for

H_2O_2 decomposition. Since CAT rapidly decomposes H_2O_2 , it serves as a useful probe to evaluate the involvement of Fe species in the H_2O_2 activation process^{48,49}. If the variation in Fe valence state is more significant without CAT than with CAT, this would indicate that Fe species participate in H_2O_2 activation. As shown in the Fe $2p$ XPS spectra, after the reaction, the Fe^{II} content in RBF1.5 decreased from 46.5 to 37.3%, while the Fe^{III} content increased from 53.5% to 62.7% (Supplementary Fig. 25a, b and Supplementary Table 2), indicating that Fe^{II} was consumed during the reaction, likely by donating electrons to activate H_2O_2 . In contrast, when CAT was added to the BF1.5 system (Supplementary Fig. 25c and Supplementary Table 2), the alterations in the contents of Fe^{II} and Fe^{III} in the post-reaction sample (BF1.5-CAT) were not more obvious than that without adding CAT, further confirming that Fe^{III} in FeOOH is efficiently reduced to Fe^{II} and participates in the activation of H_2O_2 . Accordingly, in the BF1.5 system, H_2O_2 can be activated by FeOOH to generate $\cdot\text{OH}$. Thus, $\cdot\text{OH}$ in BF1.5 is mainly derived from the activation of H_2O_2 by FNPs. The quantitative experiment of $\cdot\text{OH}$ in a closed reactor in Supplementary Fig. 26 further indicates that H_2O_2 generated by $2e^-$ WOR and $2e^-$ ORR can be both activated by FQD to generate $\cdot\text{OH}$.

Mechanism of efficient hydroxyl radical formation

To investigate the key role of FNPs in enhancing H_2O_2 activation, the surface reactivity of the catalyst was assessed through cyclic voltammetry (CV) and linear sweep voltammetry (LSV). In Supplementary Fig. 27b, a pair of $\text{Fe}^{\text{III}}/\text{Fe}^{\text{II}}$ redox peaks were observed in the CV curve of BF, indicating that FNPs in BF possess superior redox reactivity compared to pure BIO (Supplementary Fig. 27a). More importantly, negative-sweep LSV of BF revealed a decrease in overpotential and a notable increase in Fe^{III} reduction current under ultrasonic stress (Supplementary Fig. 27c), suggesting that the produced piezo-potential can further inject electrons into Fe^{III} in FNPs^{50–54}. This rapid conversion of Fe^{III} is expected to overcome the low activation efficiency of the conventional Fenton technique. The charge transfer properties of

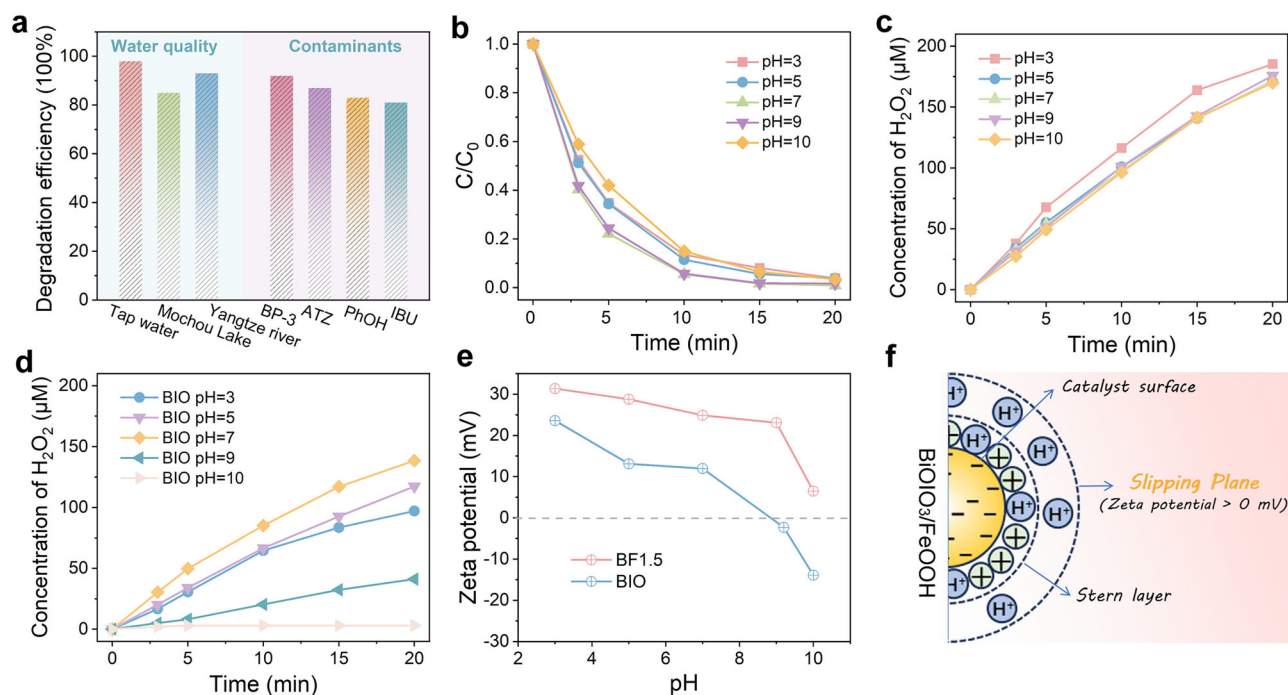


Fig. 6 | Investigation of pH-independent catalytic activity. **a** Effect of water quality and pollutant type on degradation efficiency of BF1.5. The pH adaptability for **b** RhB degradation and **c** H₂O₂ synthesis by BF1.5. **d** H₂O₂ production of BIO

under different pH conditions. **e** Zeta potential of BF1.5 and BIO under different pH conditions. **f** Scheme of H⁺ species adsorbed on the surface of BF under macro-neutral conditions.

catalysts were further investigated by photoluminescence (PL), Mott-Schottky and piezo-current response tests. In Supplementary Fig. 28, PL tests displayed a lower peak intensity of BF than that of BIO, indicating a significant suppression of electron-hole recombination, allowing more charge carriers to participate in the piezo-catalytic reaction. Furthermore, the gentler slope of BF1.5 than BIO in the Mott-Schottky diagram (Supplementary Fig. 12) demonstrates the higher charge density (Nd) and faster charge transfer in BF1.5⁴⁸. Besides, piezo-electrochemical tests visualized the piezo-current response of BIO and BF1.5 under ultrasonic vibration (Supplementary Fig. 29). BF1.5 exhibits a much higher current density, indicating the piezo-carrier can be excited and transferred to the catalyst surface more efficiently under ultrasonic stress. Clearly, the construction of spatially separated active sites accelerates carrier migration, which enable rapid electron transfer to FNPs, thus promoting the formation and activation of H₂O₂.

Density functional theory (DFT) calculations were employed to uncover the underlying mechanism of high ·OH-generating activity of BF1.5. The electronic structure of BIO and BF were initially analyzed based on DOS calculations. In Fig. 5a, the emergent Fe and O orbitals in BF resulted in electron filling around the Fermi level (E_F), which favors the ORR process^{55,56}. Further investigation into the adsorption and activation of O₂, prerequisites for the 2e⁻ ORR, was conducted through adsorption energy assessments and Bader charge analysis. Obviously, the negative adsorption energy of O₂ on BF (E_{ads} = -1.12 eV) (Fig. 5c) was well below that on BIO (E_{ads} = -0.02 eV) (Fig. 5b), demonstrating that the FNPs substantially promote O₂ adsorption. Notably, unlike the negligible charge transfer from BIO to O₂ (n = 0.007 e), substantial charge transfer from BF to surface-adsorbed O₂ occurs (n = 0.66 e), facilitating 2e⁻ ORR, consistent with the experimental results. Consequently, electron-rich FNPs serve as active sites, adsorbing O₂ and supplying electrons, thus enabling the 2e⁻ ORR process. The process of H₂O₂ activation was then studied in depth by Bader charge calculations and reaction Gibbs free energy analysis. The charge density difference diagram (Fig. 5d, e) shows the electron transfer and redistribution between H₂O₂ and catalyst. Obviously, FNPs exhibit more pronounced charge redistribution after H₂O₂ adsorption than BIO at the same iso-

surface density, indicating a stronger interaction with H₂O₂, which is conducive to H₂O₂ activation. Meanwhile, the number of electrons transferred to H₂O₂ from FNPs (0.039 e) is 3.5 times that from BIO (0.011 e), suggesting that FNPs in BF donate more electrons to the O atom in H₂O₂, facilitating its dissociation. Additionally, Fig. 5f illustrates the free energy change against the reaction coordinate for H₂O₂ activation, revealing that FNPs in BF are more favorable for the H₂O₂ decomposition into ·OH. Thus, BF is a promising candidate for piezo-self-Fenton catalysts, as its electron-rich FNPs serve as the bifunctional active center, continuously facilitating 2e⁻ ORR as well as the dissociation of H₂O₂ to ·OH.

Environmental adaptability of BF1.5 in pollutant remediation

The environmental suitability of the ·OH-dominated catalytic system is a key concern. Figure 6a and Supplementary Fig. 31 illustrate the impact of actual environmental water quality on RhB degradation by BF1.5, using tap water, Mochou Lake water, and Yangtze River water respectively. BF1.5 achieved degradation efficiencies of about 84–96% within 30 min across varying water sources, demonstrating its robust resistance to environmental interference. We further selected phenol (PhOH, a ·OH probe pollutant, $k(\cdot\text{OH}, \text{PhOH}) = 2.1 \times 10^9 \text{ M}^{-1} \text{ s}^{-1}$ ^{57–60}), along with representative recalcitrant pollutants, including benzophenone-3 (BP-3, a UV absorber), atrazine (ATZ, a pesticide), and ibuprofen (IBU, a non-steroidal anti-inflammatory drug), as target contaminants to comprehensively evaluate the pollutant degradation performance of BF1.5. The system achieved outstanding degradation efficiencies of approximately 81–93% for these pollutants within just 20 min (Fig. 6a and Supplementary Fig. 32), confirming the strong oxidizing capability of ·OH against organic pollutants.

More importantly, BF1.5 maintained a RhB degradation efficiency of over 96% across a wide pH range of pH = 3–10 (Fig. 6b), highlighting its excellent pH adaptability. This performance could be attributed to the effective H₂O₂ synthesis of BF1.5 within this pH range (Fig. 6c), which provides ample feedstock for ·OH generation. In contrast, BIO showed a sharp decline in H₂O₂ yield under alkaline conditions (Fig. 6d). This discrepancy may be attributed to the electron-rich FNPs

in BF1.5, which tend to adsorb massive H^+ species on their surface, thereby creating a surface acidic micro-environment for stable generation and activation of H_2O_2 ⁶¹. However, the accumulation of OH^- on the surface of BIO under alkaline conditions would lead to the decomposition of H_2O_2 , resulting in poor catalytic activity. Zeta potential tests corroborated the above inference (Fig. 6e), showing BF1.5 remained positively charged across pH 3–10, while BIO exhibits a negative surface charge at pH >8.8⁶². Figure 6f illustrates the potential mechanism for the pH universality of electron-rich FNPs. The Stern layer, located around the catalyst surface, consists of an ion adsorption layer formed by electrostatic attraction and van der Waals forces. The slipping layer, the outer diffusion layer of the Stern layer, is influenced by the electrode electric field, forming a loosely bound charge layer. The Zeta-potential represents the electric potential at the slipping plane. The high electron density on the surface of the FNP enhance the adsorption of hydrogen ions, thereby creating an acidic micro-environment on the catalyst surface. As a result, at pH 3–10, the BF1.5 surface exhibits a positive surface zeta potential, indicating significant adsorption of positively charged H^+ ions around the FNPs, which helps resist the effects of pH fluctuations.

Supplementary Fig. 33 demonstrates the piezo-catalytic stability of BF1.5, which retained over 90% of its piezo-degradation performance after five cycles, indicating excellent durability. Besides, the XRD and SERS spectra of the used BF1.5 catalyst show no significant changes as compared to pristine BF1.5 (Supplementary Fig. 34), demonstrating its good chemical stability. To address the challenge of recovering powder catalysts, BF1.5 was supported on nonwoven fabrics to test its piezoelectric catalytic performance. As depicted in Supplementary Fig. 35–37, the supported BF1.5 still exhibited impressive H_2O_2 yield and RhB degradation efficiency, with its performance remaining stable over multiple reaction cycles, significantly expanding its application scenarios. The exceptional water purification capacity, environmental adaptability and cyclic stability highlight the promising practical application prospects of BF1.5.

In summary, BF1.5 has been successfully developed as a piezo-self-Fenton catalyst via a controlled impregnation hydrolysis process, demonstrating high $\cdot OH$ yield and impressive pollutant degradation rates over a wide pH range. The charge redistribution between FNPs and BIO, along with continuous electron injection from piezo-catalysis, transforms FNPs into electron-rich sites. These sites continuously supply electrons to adsorbed O_2 and H_2O_2 , facilitating the $2e^-$ ORR for H_2O_2 production and its subsequent activation to $\cdot OH$. Additionally, the electron-rich FNPs promote H^+ adsorption, creating a surface-acidic microenvironment. As a result, BF1.5 excels at efficiently removing hard-to-degrade pollutants over a broad pH range. This work underscores the significance of designing environmentally adaptable catalysts capable of generating and swiftly activating H_2O_2 to drive effective environmental remediation processes.

Methods

Chemicals

All chemicals used in this work are of analytical grade and utilized without further treatment. All aqueous solutions were prepared using ultrapure water. Bismuth nitrate ($Bi(NO_3)_3 \cdot 5H_2O$), potassium iodate (KIO_3), nitric acid (65% HNO_3), tert-butanol (TBA), sodium bromates ($NaBrO_3$), 1,4-benzoquinone (p-BQ), triethanolamine (TEOA) were obtained from Sinopharm Chemical Reagent Co., Ltd. Iron triperchlorate ($Fe(ClO_4)_3 \cdot xH_2O$), Rhodamine B (RhB), benzophenone-3 (BP-3), atrazine (ATZ), phenol (PhOH) and ibuprofen (IBU) were supplied by Aladdin reagent (Shanghai) Co., Ltd., perchloric acid ($HClO_4$) was obtained from Sigma-Aldrich.

Synthesis of BIO

The $BiOIO_3$ (BIO) nanosheets were synthesized via a one-step hydrolysis method. Briefly, $Bi(NO_3)_3 \cdot 5H_2O$ (2.1 mmol) and KIO_3 (0.7 mmol)

were dispersed in a mixture of deionized water (33 mL) and 65% HNO_3 (2 mL), then stirred for 1 h at room temperature. The resulting suspension was transferred into a 50 mL Teflon-lined stainless autoclave and hydrothermally treated at 180 °C for 14 h in an electric heating oven. The sample was collected by centrifugation, washed alternately with ethanol and water, and subsequently dried at 60 °C for 10 h, yielding the white $BiOIO_3$ powder denoted as BIO.

Synthesis of BF

$BiOIO_3/FeOOH$ (BF) was synthesized by a facile impregnation hydrolysis process in acidic aqueous solution. Specifically, 50 mL deionized water was added to a beaker, then the pH was adjusted to 2.5 with perchloric acid. Next, a certain amount of ferric perchlorate was added to the above solution, following which the pH was continued to be adjusted to 2 with perchloric acid. Subsequently, 150 mg of $BiOIO_3$ catalyst was added to the above solution, dispersed homogeneously, and placed in an oil bath at 90 °C with stirring for 2 h. The powder obtained were washed to near neutrality by filtration and dried in a vacuum oven at 60 °C. The obtained samples are denoted as BF0.5, BF1.5 and BF2.5, where 0.5–2.5 indicated the mmol concentration of Fe^{III} during the preparation of BF.

Characterization

The morphology and structure of the samples were analyzed employing scanning electron microscopy (SEM, Zeiss Supra 55) and transmission electron microscopy (TEM, JEOL, JEM-2100F). X-ray diffraction (XRD, Rigaku, Smart-Lab) was utilized to determine the crystalline phase. Fourier transform infrared (FTIR) spectroscopy (Thermo Scientific Nicolet iS20) was used to study the surface functional group structure. Surface-enhanced Raman spectroscopy (SERS, LabRAM HR Evolution) was employed to analyze the chemical structure, with 514 nm laser as the excitation source. To investigate the surface states, X-ray photoelectron spectroscopy (XPS, ESCA-LAB250XI) was employed. Steady-state photoluminescence (PL) was performed using a fluorescence spectrophotometer (Hitachi, F-7000) with an excitation wavelength of 300 nm. Electron spin resonance (ESR, JES-FA200 EER) with 5,5-dimethyl-1-pyrroline N-oxide (DMPO) acting as a spin trap was used to identify active species in the samples. The diffuse reflectance absorption spectra (DRS) of the samples were examined using a UV-visible spectrophotometer (UV-3600, Shimadzu Corporation, Tokyo, Japan), with $BaSO_4$ as a reference. Additionally, surface potentials and piezoelectric properties of the produced samples were investigated using piezoelectric force microscopy (PFM) and a Kelvin probe force microscope (KPFM, Dimension Fast Scan, Bruker, America).

Quantification of hydroxyl radicals ($\cdot OH$)

The $\cdot OH$ was quantified using the terephthalic acid (TA) method. The procedure involves the reaction of TA with hydroxyl radicals to form 2-hydroxyterephthalic acid (HTA), which can be measured using fluorescence spectroscopy.

The specific steps are as follows: 20 mg of catalyst was dispersed in 50 mL mixed solution of terephthalic acid (TA) and sodium hydroxide (NaOH), with concentrations of 0.5 mM and 2 mM, respectively. The reaction was carried out under ultrasonic excitation for 20 min. At intervals, 2 mL of the supernatant was taken and tested using a fluorescence spectrophotometer, using 315 nm light for excitation. The relative content of $\cdot OH$ was determined from the fluorescence intensity of the solution at 425 nm.

Piezo-catalytic H_2O_2 generation

For the piezo-catalyzed H_2O_2 synthesis, 20 mg of the piezo-catalyst was homogeneously dispersed in 50 mL of pure water and stirred for 20 min before the reaction. The mixture was then excited by ultrasonic waves at 200 W and 40 kHz, with temperature control maintained by

circulating water during the reaction. At regular intervals, 2 mL of the clear reaction solution was withdrawn to measure the H_2O_2 yield.

The concentration of hydrogen peroxide was determined using a colorimetric method with spectrophotometry. Typically, 10 mg of peroxidase and 100 mg of N, N-diethyl-p-phenylenediamine are dissolved in 10 mL of deionized water, referred to as Solution A and Solution B, respectively. Solution C is a mixture of 10 mL of 0.1 M sodium dihydrogen phosphate (NaH_2PO_4) and 90 mL of 0.1 M disodium hydrogen phosphate (Na_2HPO_4). For the test, 1 mL of the centrifuged supernatant is added to a homogeneous mixture containing 3 mL of deionized water, 30 μL of Solution A, 30 μL of Solution B, and 300 μL of Solution C. The mixture is then shaken well, and the absorbance is measured at 551 nm using a UV-visible spectrophotometer.

Piezo-catalytic H_2O_2 generation in Ar

20 mg of piezo-catalyst was homogeneously dispersed in 50 mL of pure water and added to a sealed reactor. The reaction solution was evacuated by a vacuum pump for 30 min to remove dissolved oxygen completely. High-purity argon gas was then injected into the reactor until the pressure gauge read standard atmospheric pressure. Finally, the ultrasonic machine was turned on to activate the piezo-catalytic reaction.

Piezoelectric electrochemical measurements

The Piezoelectric electrochemical properties were tested on a CHI-660D electrochemical workstation using a standard three electrode system with Ag/AgCl electrode as the reference electrode, a Pt plate as the counter electrode, and an FTO glass covered with the prepared sample as the working electrode. Piezoelectric current, Mott-Schottky, cyclic voltammetry, and linear scanning voltammetry measurements were performed in a 0.5 M Na_2SO_4 aqueous solution.

The working electrode was prepared as follows: 8 mg of the sample was dispersed in a mixture of 960 μL of hydroalcohol (1:1) and 20 μL of naphthol (5 wt.%), and then sonicated for 60 min. Afterwards, 200 μL of the well-dispersed mixture was applied to the conductive side of the FTO glass and dried at room temperature.

Piezo-catalytic degradation of organic pollutants

20 mg of piezoelectric catalyst was homogeneously dispersed in 50 mL of contaminant solution and stirred for 30 min until adsorption-resolution equilibrium was reached. The catalyst was then excited by ultrasonic waves with 200 W at a frequency of 40 kHz for contaminant degradation. During the reaction the temperature was controlled to room temperature by circulating water. At intervals, 2 mL of the reaction solution was withdrawn and filtered through a 0.22 μm membrane, followed by ultraviolet spectrophotometry (UV) or high-performance liquid chromatography (HPLC) to detect changes in pollutant concentration during degradation, where the absorbance of RhB at 552 nm was detected by UV and the remaining several contaminants were detected by HPLC with the specific test methods shown in Supplementary Table 4. The types and concentrations of pollutants used were: [RhB] = 5 ppm, [BP-3] = 5 ppm, [ATZ] = 5 ppm, [PhOH] = 5 ppm, [BIU] = 5 ppm.

Besides, water samples were collected from the banks of Mochou Lake and Yangtze River in Nanjing, Jiangsu Province, China, to simulate the impact of real water conditions on the degradation activity of catalysts. Tap water samples were taken from the laboratory of Nanjing Hohai University.

DFT calculation

Density functional theory (DFT) calculation was performed by using the Vienna Ab-initio Simulation Package (VASP). The energy and electronic structure analysis were carried out by using VASP^{63–65} employing the projector augmented wave (PAW) method⁶⁶. The

generalized gradient approximation (GGA) of the Perdew-Burke-Ernzerh of (PBE) functional was used to treat the electronic exchange-functional⁶⁷. Van der Waals (vdW) interaction was described using Grimme's semi-empirical dispersion-corrected DFT-D3 method. A plane-wave basis set with k point of $1 \times 1 \times 1$, cutoff energy with 450 eV, and energy convergence criteria with 10^{-5} eV, and the forces on each atom were less than 0.03 eV \AA^{-1} . The following formula was used to calculate the free energy (ΔG) of the piezo-catalytic reaction step:

$$G(T) = E_{\text{ele}} + G_{\text{corr}}(T) = E_{\text{ele}} + \text{ZPE} + \Delta G_{0 \rightarrow T} \quad (1)$$

where E_{ele} , $G_{\text{corr}}(T)$, ZPE and $G_{0 \rightarrow T}$ stand for electronic energy, thermal corrections to Gibbs free energy, zero-point energy and contribution by heating the system from 0 K to 298.15 K, respectively.

The load of catalysts on non-woven fabric

The BF1.5-loaded polypropylene non-woven fabric was prepared by the hot-melt embedding method. Typically, 50 mg of BF1.5 catalyst was dispersed into 10 mL of ethanol and sonicated for 1 h to form a mixed solution, which was subsequently filled into small spray bottles. Spray the mixture solution in the spray bottle evenly onto the square polypropylene non-woven fabric (2×2 cm), dry naturally, and repeat this step three times. Afterwards, the iron is heated to about 170 $^{\circ}\text{C}$ to iron the non-woven fabrics, until the surface of the nonwoven fabrics appears to be melted, then stop ironing, and the catalyst can be firmly embedded in the surface of the nonwoven fabrics after cooling naturally. Repeat this operation until the catalyst is fully embedded. Finally, BF1.5 catalyst-loaded non-woven fabric was washed well with pure water to remove the surface of unfastened catalysts.

Data availability

The data supporting the plots within this paper and other study findings are available from the corresponding author upon request. The data generated in this study are provided in the Supplementary Information/Source Data file. Source data are provided with this paper.

References

- Nosaka, Y. & Nosaka, A. Y. Generation and detection of reactive oxygen species in photocatalysis. *Chem. Rev.* **117**, 11302–11336 (2017).
- Meyerstein, D. Re-examining Fenton and Fenton-like reactions. *Nat. Rev. Chem.* **5**, 595–597 (2021).
- Jin, C. C., Liu, D. M. & Zhang, L. X. An emerging family of piezo-catalysts: 2D piezoelectric materials. *Small* **19**, 2303586 (2023).
- Zhang, P. et al. Kinetic models for hydroxyl radical production and contaminant removal during soil/sediment oxygenation. *Water Res.* **240**, 120071 (2023).
- Wardman, P. Reduction potentials of one-electron couples involving free radicals in aqueous solution. *J. Phys. Chem. Ref. Data* **18**, 1637–1755 (1989).
- Mendez-Arriaga, F., Esplugas, S. & Gimenez, J. Degradation of the emerging contaminant ibuprofen in water by photo-Fenton. *Water Res.* **44**, 589–595 (2010).
- Hou, X. et al. Hydroxylamine promoted goethite surface Fenton degradation of organic pollutants. *Environ. Sci. Technol.* **51**, 5118–5126 (2017).
- Hang, J. et al. Heterogeneous photo-Fenton degradation toward sulfonamide matrix over magnetic Fe_3S_4 derived from MIL-100 (Fe). *J. Hazard. Mater.* **424**, 127415 (2022).
- Nosaka, Y. & Nosaka, A. Understanding hydroxyl radical ($\cdot\text{OH}$) generation processes in photocatalysis. *ACS Energy Lett.* **1**, 356–359 (2016).
- Wen, Y. et al. Interface interaction enhanced piezo-catalytic hydrogen peroxide generation via one-electron water oxidation. *ACS Energy Lett.* **33**, 2308084 (2023).

11. Chatel, G. & Colmenares, J. C. Sonochemistry: from basic principles to innovative applications. *Top. Curr. Chem.* **375**, 1–4 (2017).
12. Wang, F. et al. Unprecedentedly efficient mineralization performance of photocatalysis-self-Fenton system towards organic pollutants over oxygen-doped porous g-C₃N₄ nanosheets. *Appl. Catal. B Environ.* **312**, 121438 (2022).
13. Zhang, K. et al. Near-complete suppression of oxygen evolution for photoelectrochemical H₂O oxidative H₂O₂ synthesis. *J. Am. Chem. Soc.* **142**, 8641–8648 (2020).
14. Xie, J., Zhang, C. & Waite, T. D. Hydroxyl radicals in anodic oxidation systems: generation, identification and quantification. *Water Res.* **217**, 118425 (2022).
15. Che, H. et al. Iodide-induced fragmentation of polymerized hydrophilic carbon nitride for high-performance quasi-homogeneous photocatalytic H₂O₂ production. *Angew. Chem. Int. Ed.* **60**, 25546–25550 (2021).
16. Liu, W. et al. Unraveling the mechanism on ultrahigh efficiency photocatalytic H₂O₂ generation for dual-heteroatom incorporated polymeric carbon nitride. *Adv. Funct. Mater.* **32**, 2205119 (2022).
17. Lee, B.-H. et al. Supramolecular tuning of supported metal phthalocyanine catalysts for hydrogen peroxide electrosynthesis. *Nat. Catal.* **6**, 234–243 (2023).
18. Wei, Y., Zhang, Y., Miao, J., Geng, W. & Long, M. In-situ utilization of piezo-generated hydrogen peroxide for efficient p-chlorophenol degradation by Fe loading bismuth vanadate. *Appl. Surf. Sci.* **543**, 148791 (2021).
19. Luo, M. et al. An integrated catalyst of Pd supported on magnetic Fe₃O₄ nanoparticles: simultaneous production of H₂O₂ and Fe²⁺ for efficient electro-Fenton degradation of organic contaminants. *Water Res.* **48**, 190–199 (2014).
20. Kavitha, V. & Palanivelu, K. The role of ferrous ion in Fenton and photo-Fenton processes for the degradation of phenol. *Chemosphere* **55**, 1235–1243 (2004).
21. Goldstein, S., Meyerstein, D. & Czapski, G. The Fenton reagents. *Free Radic. Bio. Med.* **15**, 435–445 (1993).
22. Zhang, X. et al. Nanoconfinement-triggered oligomerization pathway for efficient removal of phenolic pollutants via a Fenton-like reaction. *Nat. Commun.* **15**, 917 (2024).
23. Li, J., Pham, A. N., Dai, R., Wang, Z. & Waite, T. D. Recent advances in Cu-Fenton systems for the treatment of industrial wastewaters: role of Cu complexes and Cu composites. *J. Hazard. Mater.* **392**, 122261 (2020).
24. Zhou, X. et al. Identification of Fenton-like active Cu sites by heteroatom modulation of electronic density. *Proc. Natl. Acad. Sci. USA* **119**, e2119492119 (2022).
25. Yamaguchi, R., Kurosu, S., Suzuki, M. & Kawase, Y. Hydroxyl radical generation by zero-valent iron/Cu (ZVI/Cu) bimetallic catalyst in wastewater treatment: Heterogeneous Fenton/Fenton-like reactions by Fenton reagents formed in-situ under oxic conditions. *Chem. Eng. J.* **334**, 1537–1549 (2018).
26. Liu, Y. & Wang, J. Multivalent metal catalysts in Fenton/Fenton-like oxidation system: a critical review. *Chem. Eng. J.* **466**, 143147 (2023).
27. Zhang, W. et al. Spatially asymmetric catalyst design with electron-rich Cu sites to facilitate full-spectrum photo-Fenton-like catalysis. *Chem. Catal.* **5**, 101358 (2025).
28. Xu, J., Che, H., Tang, C., Liu, B. & Ao, Y. Tandem fields facilitating directional carrier migration in Van der Waals heterojunction for efficient overall Piezo-synthesis of H₂O₂. *Adv. Mater.* **36**, 2404539 (2024).
29. Cornell, R. M., Giovanoli, R. & Schneider, W. Review of the hydrolysis of iron (III) and the crystallization of amorphous iron (III) hydroxide hydrate. *J. Chem. Technol. Biot.* **46**, 115–134 (1989).
30. Li, P. et al. Multiscale structural engineering of a multilayered nanoarray electrode realizing boosted and sustained oxygen evolution catalysis in seawater electrolysis. *ACS Catal.* **13**, 15360–15374 (2023).
31. Liu, M., Qiu, X., Miyauchi, M. & Hashimoto, K. Energy-level matching of Fe (III) ions grafted at surface and doped in bulk for efficient visible-light photocatalysts. *J. Am. Chem. Soc.* **135**, 10064–10072 (2013).
32. Tang, J. et al. Double-shelled porous g-C₃N₄ nanotubes modified with amorphous Cu-doped FeOOH nanoclusters as OD/3D non-homogeneous photo-fenton catalysts for effective removal of organic dyes. *Small* **19**, 2208232 (2023).
33. Zeng, Y. et al. Iron-based supercapacitor electrodes: advances and challenges. *Adv. Energy Mater.* **6**, 1601053 (2016).
34. Liu, J., Zheng, M., Shi, X., Zeng, H. & Xia, H. Amorphous FeOOH quantum dots assembled mesoporous film anchored on graphene nanosheets with superior electrochemical performance for supercapacitors. *Adv. Funct. Mater.* **26**, 919–930 (2016).
35. Shi, M., Xiao, P., Lang, J., Yan, C. & Yan, X. Porous g-C₃N₄ and MXene dual-confined FeOOH quantum dots for superior energy storage in an ionic liquid. *Adv. Sci.* **7**, 1901975 (2020).
36. Qian, X. et al. FeOOH quantum dots coupled g-C₃N₄ for visible light driving photo-Fenton degradation of organic pollutants. *Appl. Catal. B Environ.* **237**, 513–520 (2018).
37. M. Ristić, S., Musić, S. & Godec, M. Properties of γ-FeOOH, α-FeOOH and α-Fe₂O₃ particles precipitated by hydrolysis of Fe³⁺ ions in perchlorate containing aqueous solutions. *J. Alloy. Compd.* **417**, 292–299 (2006).
38. Luo, W. et al. Highly crystallized α-FeOOH for a stable and efficient oxygen evolution reaction. *J. Mater. Chem. A* **5**, 2021–2028 (2017).
39. Chen, Y. C. et al. Novel iron oxyhydroxide lepidocrocite nanosheet as ultrahigh power density anode material for asymmetric supercapacitors. *Small* **10**, 3803–3810 (2014).
40. Gao, X., Ma, C., Liu, Y., Xing, L. & Yan, Y. Self-induced Fenton reaction constructed by Fe (III) grafted BiVO₄ nanosheets with improved photocatalytic performance and mechanism insight. *Appl. Surf. Sci.* **467**, 673–683 (2019).
41. Chen, F. et al. Macroscopic spontaneous polarization and surface oxygen vacancies collaboratively boosting CO₂ photoreduction on BiOI/O₃ single crystals. *Adv. Mater.* **32**, 1908350 (2020).
42. Liu, S. et al. A top-down strategy for amorphization of hydroxyl compounds for electrocatalytic oxygen evolution. *Nat. Commun.* **13**, 1187 (2022).
43. Liu, Y. et al. Low overpotential in vacancy-rich ultrathin CoSe₂ nanosheets for water oxidation. *J. Am. Chem. Soc.* **136**, 15670–15675 (2014).
44. Xu, J. et al. Highly efficient Fe^{III}-initiated self-cycled Fenton system in piezo-catalytic process for organic pollutants degradation. *Angew. Chem. Int. Ed.* **62**, e202307018 (2023).
45. Zhang, Q., Che, H., Yang, H., Liu, B. & Ao, Y. Tandem proton transfer in carboxylated supramolecular polymer for highly efficient overall photosynthesis of hydrogen peroxide. *Angew. Chem. Int. Ed.* **63**, e202409328 (2024).
46. Chen, L. et al. Acetylene and diacetylene functionalized covalent triazine frameworks as metal-free photocatalysts for hydrogen peroxide production: a new two-electron water oxidation pathway. *Adv. Mater.* **32**, 1904433 (2020).
47. Wang, L. et al. A polymer tethering strategy to achieve high metal loading on catalysts for Fenton reactions. *Nat. Commun.* **14**, 7841 (2023).
48. Ran, M. et al. Dynamic defects boost in-situ H₂O₂ piezocatalysis for water cleanup. *Proc. Natl. Acad. Sci. USA* **121**, e2317435121 (2024).
49. Jiang, H. et al. Electron donor-acceptor activated anti-Fenton property for the ultradurable oxygen reduction reaction. *ACS Nano* **19**, 12161–12169 (2025).

50. Chai, M. et al. Piezoelectric-Fenton degradation and mechanism study of Fe₂O₃/PVDF-HFP porous film drove by flowing water. *J. Hazard. Mater.* **430**, 128446 (2022).
51. Ge, L. et al. A Piezo-Fenton system with rapid iron cycling and hydrogen peroxide self-supply driven by ultrasound. *Chem. Eur. J.* **28**, e202202494 (2022).
52. Su, C., Li, C., Li, R. & Wang, W. Insights into highly efficient piezo-catalytic molecule oxygen activation over Bi₂Fe₄O₉: active sites and mechanism. *Chem. Eng. J.* **452**, 139300 (2023).
53. Hou, K. et al. Sulfide enhances the Fe (II)/Fe (III) cycle in Fe (III)-peroxymonosulfate system for rapid removal of organic contaminants: treatment efficiency, kinetics and mechanism. *J. Hazard. Mater.* **435**, 128970 (2022).
54. Hou, K. et al. Trace-dissolved S (-II) triggers the Fe (III)-activated H₂O₂ process for organic pollutant degradation by promoting the Fe (III)/Fe (II) cycle: kinetics, toxicity, and mechanisms. *ACS EST Eng.* **2**, 2174–2186 (2022).
55. Wang, K. et al. Kinetically controlled, scalable synthesis of γ-FeOOH nanosheet arrays on nickel foam toward efficient oxygen evolution: the key role of in-situ-generated γ-NiOOH. *Adv. Mater.* **33**, 2005587 (2021).
56. Huang, H. et al. Tailoring oxygen reduction reaction kinetics on perovskite oxides via oxygen vacancies for low-temperature and knittable zinc–air batteries. *Adv. Mater.* **35**, 2303109 (2023).
57. Wang, Z. et al. Is sulfate radical really generated from perox-ydisulfate activated by iron (II) for environmental decontamination?. *Environ. Sci. Technol.* **52**, 11276–11284 (2018).
58. Dong, H. et al. Degradation of organic contaminants in the Fe (II)/peroxymonosulfate process under acidic conditions: the over-looked rapid oxidation stage. *Environ. Sci. Technol.* **55**, 15390–15399 (2021).
59. De, A. K., Chaudhuri, B., Bhattacharjee, S. & Dutta, B. K. Estimation of ·OH radical reaction rate constants for phenol and chlorinated phenols using UV/H₂O₂ photo-oxidation. *J. Hazard. Mater.* **64**, 91–104 (1999).
60. Field, R., Raghavan, N. & Brummer, J. A pulse radiolysis investigation of the reactions of bromine dioxide radical (BrO₂·) with hexacyanoferrate (II), manganese (II), phenoxide ion, and phenol. *J. Phys. Chem.* **86**, 2443–2449 (1982).
61. Tan, H. et al. Engineering a local acid-like environment in alkaline medium for efficient hydrogen evolution reaction. *Nat. Commun.* **13**, 2024 (2022).
62. Liu, X. et al. Low frequency hydromechanics-driven generation of superoxide radicals via optimized piezotronic effect for water disinfection. *Nano Energy* **88**, 106290 (2021).
63. Kresse, G. & Hafner, J. Ab initio molecular dynamics for liquid metals. *Phys. Rev. B* **47**, 558 (1993).
64. Kresse, G. & Hafner, J. Ab initio molecular-dynamics simulation of the liquid-metal–amorphous-semiconductor transition in germanium. *Phys. Rev. B* **49**, 14251 (1994).
65. Kohn, W. & Sham, L. J. Self-consistent equations including exchange and correlation effects. *Phys. Rev.* **140**, A1133 (1965).
66. Blöchl, P. E. Projector augmented-wave method. *Phys. Rev. B* **50**, 17953 (1994).
67. Perdew, J. P., Burke, K. & Ernzerhof, M. Generalized gradient approximation made simple. *Phys. Rev. Lett.* **77**, 3865 (1996).

Acknowledgements

We are grateful for grants from the National Key Research and Development Program of China (2022YFC3202402), Fundamental Research Funds for Cornell University (B230205044), Natural Science Foundation of China (52100179, T2322013), Fundamental Research Funds for the Central Universities (B240201082 and B200202103), Priority Academic Program Development of Jiangsu Higher Education Institutions.

Author contributions

J.X. and Y.A. conceived and designed the experiments. J.X. carried out the experimental operations and data analysis. K.G. participated in part of the experimental operations and analysis. P.W., P.C., and H.C. participated in part of the materials synthesis and provided suggestions for the optimization of the experiments. C.T. provided theoretical calculation guidance. J.X., Y.A., and K.Z. co-wrote the paper. All authors discussed the results and commented on the manuscript.

Competing interests

The authors declare no competing interests.

Additional information

Supplementary information The online version contains supplementary material available at <https://doi.org/10.1038/s41467-025-63337-x>.

Correspondence and requests for materials should be addressed to Kan Zhang or Yanhui Ao.

Peer review information *Nature Communications* thanks the anonymous reviewers for their contribution to the peer review of this work. A peer review file is available.

Reprints and permissions information is available at <http://www.nature.com/reprints>

Publisher's note Springer Nature remains neutral with regard to jurisdictional claims in published maps and institutional affiliations.

Open Access This article is licensed under a Creative Commons Attribution-NonCommercial-NoDerivatives 4.0 International License, which permits any non-commercial use, sharing, distribution and reproduction in any medium or format, as long as you give appropriate credit to the original author(s) and the source, provide a link to the Creative Commons licence, and indicate if you modified the licensed material. You do not have permission under this licence to share adapted material derived from this article or parts of it. The images or other third party material in this article are included in the article's Creative Commons licence, unless indicated otherwise in a credit line to the material. If material is not included in the article's Creative Commons licence and your intended use is not permitted by statutory regulation or exceeds the permitted use, you will need to obtain permission directly from the copyright holder. To view a copy of this licence, visit <http://creativecommons.org/licenses/by-nc-nd/4.0/>.

© The Author(s) 2025